
Dynamic Responses of a Tower Crane Tower and Payload Subjected to Elastic Jib in Radial Motion

Ruiqi Gao and Mingxiao Dong

Shandong Jianzhu University, Shandong, 250101, China. E-mail: mxdong@sdjzu.edu.cn

Dalong He

Shandong Longhui Lifting Machinery Co, Ltd, Shandong, 271224, China.

Runhui Feng

South China University of Technology, Guangdong, 510640, China.

(Received 19 December 2022; accepted 28 April 2023)

Due to slender truss structures, the tower and jib of tower cranes can easily produce vibrations during the acceleration and deceleration of the motion. The alternating load generated by this vibration reduces the payload's positioning accuracy and is also one of the main factors to cause fatigue damage to the crane structure. Based on the Euler-Bernoulli beam theory, this paper derives the differential equations of tower vibration, jib vibration, and payload swing under the radial motion by the Lagrangian equation. The vibration modes of the tower are analyzed, and the effect of trolley speed, payload mass, and rope length on the vibration characteristics of the tower and the payload swing characteristics subjected to elastic jib is studied through simulation. The expression of the maximum swing angle is derived, and the experiment verifies the validity of the simulation results.

1. INTRODUCTION

The structure of a tower crane includes the tower, jib, counter jib, and tower cap, which are welded or bolted together using standard sections. The lifting, radial and slewing motions are used to describe the process of transporting payloads. The frequent starting and braking of the three motions cause structural vibration and payload swing.¹ The tower overturning caused by alternating low-cycle loads can result in significant economic losses.²

There is a large body of literature investigating structural vibration and payload swing. Oliveira et al.³⁻⁵ modeled a tower crane using finite element software, and Chen⁶ simulated the finite element model of a tower crane using computational fluid dynamics (CFD) to obtain the maximum displacement, bending stress, and axial stress under a pulsating wind load. Although the finite element model is effective for investigating the wind load characteristics of a tower crane, it cannot obtain dynamic responses in traveling motions.

Thus, some papers have studied structural vibrations by constructing mathematical models of cranes. The linear partial differential equations for the vibration of the main beam can be obtained by considering the bridge crane as a simply supported beam with a moving mass.⁷⁻⁹ Azam¹⁰ created differential equations for the vibrations of a Timoshenko beam with the moving mass based on the Hamiltonian principle and obtained solutions by the numerical method. The model proposed above will cause a significant error in the analysis of the tower vibration because the coupling of the flexible jib should be taken into account.

Considering the effect of other equipment ensembles on the vibration of the structure along the elastic cable, Debeleac¹¹ presented a novel computational model that helps to study the dynamics of a dragline bucket. The results showed the cou-

pling terms between drag and hoist dynamics with the influence of the bucket. In the following work,¹² the model of the dragline bucket system was improved, and the differential equations governing the drag cable oscillations were analyzed using the tensile force within the hoist cable. It provides the basis for investigating structural damage to the wire rope.¹³ Given the more significant interaction between flexible-link elements and payload swing, the above approaches may not apply to tower cranes.

Rauscher and Sawodny¹⁴ presented that the tower crane jib was modeled as a distributed-mass beam considering the Coriolis force in a slewing motion. Nevertheless, it does not focus on the dynamic effects of some indicators on the structural vibration characteristics during the working cycle. Based on the Euler-Bernoulli beam theory, Feng¹⁵ assumed that the tower is a rigid body and obtained the differential equations of the jib-trolley-load system using Lagrange's equation. However, the jib is a cantilever beam with simple boundary conditions, while the tower needs to consider the effect of the translational and rotational inertia of the slewing structure.

This paper proposes an analytical approach for simulating the tower vibration, payload swing, and jib vibration of a tower crane in radial motion. Considering dynamic couplings with structural inertia, vibration, and the payload swing in the numerical model, qualitative indicators of the vibration characteristics of the element components are analyzed. The tower and jib are discretized by the Ritz method of modal shapes, which leads to a significant increase in coupling effects. Therefore, it is a challenge to solve complex multi-body dynamic equations.

In Section 2, the numerical model of a tower crane is established. Then, the differential equations are derived from Lagrange's equation. Section 3 performs the modal analysis of the tower. Section 4 uses Matlab software to simulate the

effect of dynamic responses of tower vibration and payload swing. Section 5 designs experiments to verify the simulation results.

2. DIFFERENTIAL EQUATIONS OF THE SYSTEM

The research object is a QTZ5613 flat-head tower crane. Only the tower vibration and the payload swing subjected to an elastic jib are investigated in the radial motion. Therefore, the payload swing excites the tower and the jib, producing vibrations only in the vertical plane of the jib. The jib is equivalent to a horizontal cantilever with a moving mass, and the tower is equivalent to a plumb beam.¹⁶

2.1. Coordinate System

According to the characteristics of the slewing motion and the radial motion, an inertial coordinate system $\{x_0, y_0, z_0\}$ is established. The coordinate origin is chosen at the intersection of the tower's centerline and the jib's slewing plane. A non-inertial coordinate system $\{x, y, z\}$ is established to describe the displacement of the tower and jib. The origin coincides with the origin of the inertial coordinate system. Since the payload moves with the suspension point in the swing motion, a non-inertial spherical coordinate system $\{e_l, e_\theta, e_\phi\}$ is established with the suspension point on the trolley as the coordinate origin. The displacement of the structures and payload swing angles at xoz -plane and in y -direction are shown in Fig. 1 and Fig. 2, respectively.

In Fig. 1, $\gamma(t)$ is the pitch angle of the jib due to the displacement of the tower. $V_x(z, t)$ and $W_z(x, t)$ represent the displacement of the tower in x -direction and the jib in z -direction at time t , respectively.

In Fig. 2, the swing angle of the jib is $\psi(t)$. $V_y(z, t)$ and $W_y(x, t)$ represent the displacement of the tower and jib at time t in y -direction respectively. The position of the suspension point in $\{x, y, z\}$ is $(x_c, y_c, 0)$, and x_c is the vertical distance from the trolley to the centerline of the tower. The position of the payload in $\{e_l, e_\theta, e_\phi\}$ is defined as (l, θ, ϕ) , where l is the length of the rope, θ is the angle between the projection of the rope at the xoz -plane and the plumb line of the suspension point, and ϕ represents the angle between the rope and the xoz -plane.

2.2. Energy Expressions

This paper assumes that the tower and jib have no longitudinal deformation and that the counter jib is rigid. There is no relative sliding between the trolley and the jib,¹⁵ and the rope is rigid with the length constant.¹⁷ Using the Ritz method,¹⁶ the deformation of the tower and jib can be expressed as follows:

$$\begin{aligned} V_x(z, t) &= \sum_{i=1}^n \varphi_{t,i}(z)q_{t,i}(t) \\ W_z(x, t) &= \sum_{i=1}^n \varphi_{b,i}(x)q_{b,i}(t); \end{aligned} \tag{1}$$

where $\varphi_{t,i}$ and $\varphi_{b,i}$ are the i^{th} mode shape of the tower and jib, respectively. $q_{t,i}$ and $q_{b,i}$ are the generalized coordinates

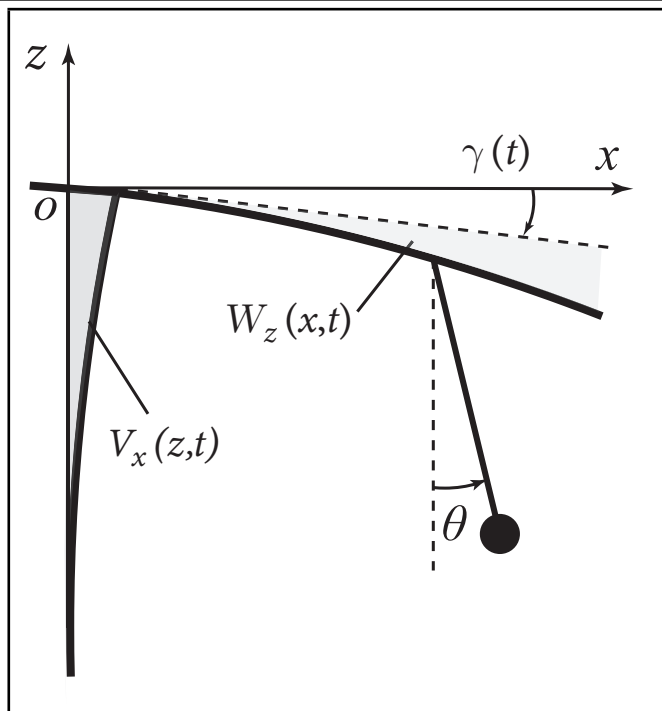


Figure 1. Displacement of structures and payload swing in xoz -plane.

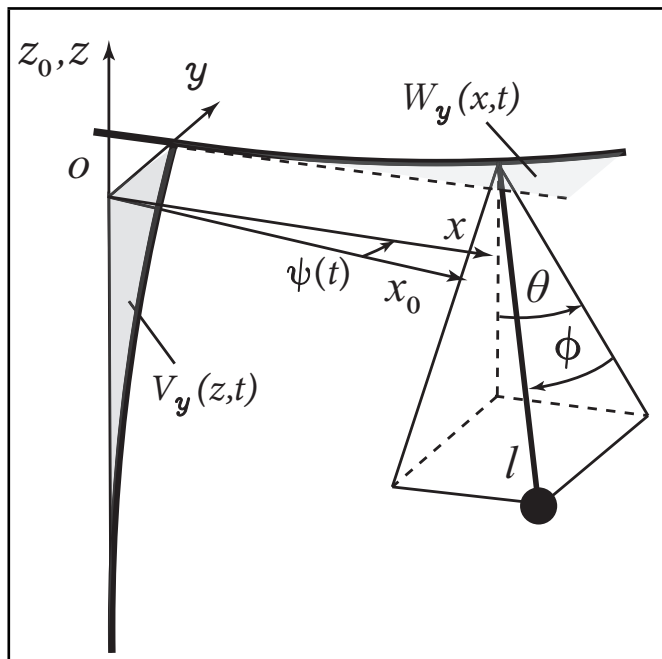


Figure 2. Displacement of structures payload swing in y -direction.

which are time-dependent functions and n is the number of coordinates.

(1) Tower

The position vector of the tower unit in the inertial coordinate system is:

$$r_t = [V_x(z, t) \quad V_y(z, t) \quad z]^T T_z^T r_o; \tag{2}$$

where z is the position of the tower unit, $z \in [-l_t, 0]$, l_t is the height of the tower. $r_o = [i \quad j \quad k]^T$ is the basis vector in the inertial coordinate.

T_z , seen in Appendix Eq. (A1), is the transformation matrix which denotes the coordinate system $\{x, y, z\}$ rotated around the z -axis into $\{x_0, y_0, z_0\}$.

The kinetic energy of the tower is:

$$K_t = \frac{1}{2} \int_{-l_t}^0 m_t |\dot{r}_t(z, t)|^2 dz; \quad (3)$$

where m_t is the mass of the tower unit. In the radial motion, $V_y(z, t) = 0$ and T_z is third-order identity matrix. Substituting the Eq. (2) into Eq. (3), yields:

$$K_t = \frac{1}{2} \sum_{i=1}^n \sum_{j=1}^n \dot{q}_{t,i} \dot{q}_{t,j} \int_{-l_t}^0 m_t \varphi_{t,i}(z) \varphi_{t,j}(z) dz; \quad (4)$$

(2) Jib and counter jib

Both the jib and the counter jib are defined as the same form of position vector in the inertial coordinate

$$r_b(x, t) = r_t(0, t) + [x_b \quad W_y(x, t) \quad W_z(x, t)] T_z^T T_y^T r_o$$

$$r_{cb}(x, t) = r_b(x_{cb}, t); \quad (5)$$

where T_y , seen in Appendix Eq. (A1), is the transformation matrix of the jib and counter jib position vector around the y -axis into the coordinate system $\{x, y, z\}$. x_b and x_{cb} are the position of the jib and counter jib unit, respectively. $x_b \in [0, l_b]$, $x_{cb} \in [-l_{cb}, 0]$, l_b and l_{cb} are the length of the jib and the counter jib, respectively. $W_y(z, t) = 0$ and T_z is third-order identity matrix. The position vectors of the jib and counter jib are defined as:

$$r_b(x, t) = \begin{bmatrix} \cos \gamma x_b + \sin \gamma W_z + V_x(0, t) \\ W_y + V_y(0, t) \\ -\sin \gamma x_b + \cos \gamma W_z \end{bmatrix} r_o;$$

$$r_{cb}(x, t) = \begin{bmatrix} \cos \gamma x_{cb} + V_x(0, t) \\ V_y(0, t) \\ -\sin \gamma x_{cb} \end{bmatrix} r_o; \quad (6)$$

the kinetic energy of jib and counter jib are defined as:

$$K_b = \frac{1}{2} \int_0^{l_b} m_b(x) |\dot{r}_b(x, t)|^2 dx;$$

$$K_{cb} = \frac{1}{2} \int_{-l_{cb}}^0 m_{cb}(x) |\dot{r}_{cb}(x, t)|^2 dx; \quad (7)$$

where m_b and m_{cb} are the mass of jib and counter jib unit, respectively. Substituting Eq. (6) into Eq. (7), yields:

$$K_b = \sum_{i=1}^n \sum_{j=1}^n \dot{q}_{b,i} \dot{q}_{b,j} \int_0^{l_b} m_b \varphi_{b,i}(x) \varphi_{b,j}(x) dx$$

$$+ \frac{1}{2} m_b l_b [\dot{V}_x(0, t) + V'_x(0, t) W_z(x_b)]^2$$

$$+ \frac{1}{2} \int_0^{l_b} m_b W_z(x_b)^2 dx [\dot{V}'_x(0, t)]^2 + \frac{1}{2} J_b [\dot{V}'_x(0, t)]^2;$$

$$K_{cb} = \frac{1}{2} m_{cb} l_{cb} [\dot{V}_x(0, t)]^2 + \frac{1}{2} J_{cb} [\dot{V}'_x(0, t)]^2; \quad (8)$$

where $dV_x/dt = \dot{V}_x$ is the derivative with respect to time, and $dV_x/dx = V'_x$ is the derivative with respect to x .

$J_b = \frac{1}{2} \int_0^{l_b} m_b x_b^2 dx$ and $J_{cb} = \frac{1}{2} \int_{-l_{cb}}^0 m_{cb} x_{cb}^2 dx$ are the rotational inertia of jib and counter jib due to the pitch motion, respectively.

(3) Counter weight

The counter weight is equivalent to a mass m_{cw} at the counter jib end, with a position vector of:

$$r_{cw}(x, t) = r_{cb}(-l_{cb}, t); \quad (9)$$

the kinetic energy of the counter weight is defined as:

$$K_{cw} = \frac{1}{2} m_{cw} [\dot{V}_x^2(0, t)] + \frac{1}{2} J_{cb} [\dot{V}'_x(0, t)]^2; \quad (10)$$

where m_{cw} is the mass of the counter weight, $J_{cw} = \frac{1}{2} m_{cw} l_{cb}^2$ is the rotational inertia of the counter weight. The kinetic energy of the tower crane structures can be defined as:

$$K_s = K_t + K_b + K_{cb} + K_{cw}; \quad (11)$$

(4) Trolley and payload

The trolley is equivalent to the moving mass on the jib, and its position vector and energy expressions are defined as:

$$r_c = r_b(x_c, t);$$

$$r_c = T_z \begin{bmatrix} \cos \gamma x_c + \sin \gamma W_z + V_x(0, t) \\ W_y + V_y(0, t) \\ -\sin \gamma x_c + \cos \gamma W_z \end{bmatrix} r_o; \quad (12)$$

$$K_c = \frac{1}{2} m_c |\dot{r}_c|^2;$$

$$U_c = m_c [0 \quad 0 \quad g]^T r_c;$$

where m_c is the trolley mass, K_c and U_c are the kinetic energy and potential energy of the trolley respectively. The pendulum angle of the payload $\phi = 0$. The expressions of the payload position vector and energy are defined as:

$$r_p = r_c + [0 \quad 0 \quad -l] T_G^T T_z^T r_o;$$

$$r_p = T_z \begin{bmatrix} \cos \gamma x_c + \sin \gamma W_z + V_x(0, t) - l \sin \theta \\ W_y + V_y(0, t) \\ -\sin \gamma x_c + \cos \gamma W_z - l \cos \theta \end{bmatrix} r_o;$$

$$K_p = \frac{1}{2} m_p |\dot{r}_p|^2;$$

$$U_p = m_p [0 \quad 0 \quad g]^T r_p; \quad (13)$$

where m_p is the payload mass, K_p and U_p are the kinetic energy and potential energy of the payload respectively. T_G , seen in Appendix Eq. (A1), is the coordinate transformation matrix of the spherical coordinate $\{e_l, e_\theta, e_\phi\}$ into the coordinate $\{x, y, z\}$.

2.3. Differential Equations for Structural Vibration and Payload Swing

The total kinetic energy of the system includes the kinetic energy of the structures, trolley, and payload, so it is defined as:

$$K_{tot} = K_s + K_c + K_p; \quad (14)$$

more details are shown in Appendix Eq. (A2). The total potential energy of the system is defined as:¹⁶

$$\begin{aligned}
 U_{\text{tol}} &= U_s + U_c + U_p \\
 &= \frac{1}{2} \sum_i^n [\omega_{t,i} q_{t,i}(t)]^2 + \sum_i^n [\omega_{b,i} q_{b,i}(t)]^2 \\
 &\quad + m_c g \left[-x_c \sum_i^n \varphi'_{t,i}(0) q_{t,i}(t) + W_z(x_c) \right] \\
 &\quad + m_p g \left[-x_c \sum_i^n \varphi'_{t,i}(0) q_{t,i}(t) + W_z(x_c) - l \cos \theta \right]; \quad (15)
 \end{aligned}$$

where U_s is the elastic strain energy of tower and jib. $\omega_{t,i}$ and $\omega_{b,i}$ are the i^{th} intrinsic frequency of the tower and jib, respectively.

The generalized damping force of the rope-loading mass ensemble can be characterized as $Q_d = -D_l(\delta)\dot{l}$,¹⁸ where $D_l(\delta)$ is the damping matrix with respect to the damping ratio δ calculated from the experimental data.¹⁹ Thus, the Lagrangian equation for the tower crane system is defined as:

$$\frac{d}{dt} \left(\frac{\partial L}{\partial \dot{\eta}_i^*} \right) - \frac{\partial L}{\partial \eta_i^*} = Q_i + Q_d, \quad (i = 1, 2, 3 \dots); \quad (16)$$

where, $L = K_{\text{tol}} - U_{\text{tol}}$ is the Lagrangian function, $\eta_i^* = [q_{t,i}, q_{b,i}, \theta]$ is the generalized coordinates in the radial motion, $\dot{\eta}_i^*$ is the generalized velocity and Q_i is the generalized excitation force of external action.

Substituting Eq. (14) and Eq. (15) into Eq. (16) to find the differential equations with respect to the generalized coordinate $q_{t,i}$, $q_{b,i}$ and θ , respectively, yields:

$$\begin{aligned}
 &\ddot{q}_{t,i}(t) + \omega_{t,i} q_{t,i}(t) + (m_c + m_p) \varphi'_{t,i}(0) x_c \\
 &\left(\ddot{x}_c \sum_{i=1}^n \varphi'_{t,i}(0) q_{t,i}(t) + 2\dot{x}_c \sum_{i=1}^n \varphi'_{t,i}(0) \dot{q}_{t,i}(t) + x_c \sum_{i=1}^n \varphi'_{t,i}(0) \ddot{q}_{t,i}(t) \right) \\
 &\quad + (m_c + m_p) \varphi_{t,i}(0) \left(\sum_{i=1}^n \varphi_{t,i}(0) \ddot{q}_{t,i}(t) + \ddot{x}_c \right) \\
 &\quad - m_p \varphi_{t,i}(0) l x_c (\cos \theta \ddot{\theta} - \sin \theta \dot{\theta}^2) - (m_c + m_p) g x_c \varphi'_{t,i}(0) \\
 &\quad - m_p \varphi'_{t,i}(0) l x_c (\cos \theta \dot{\theta} + \sin \theta \ddot{\theta}) \\
 &+ \left[2(m_c + m_p) W_z(x_c)^2 + \sum_{i=1}^n q_{b,i}(t)^2 \right] \varphi'_{t,i}(0) \sum_{i=1}^n \varphi'_{t,i}(0) \dot{q}_{t,i}(t) = 0; \quad (17)
 \end{aligned}$$

$$\begin{aligned}
 &\ddot{q}_{b,i}(t) + \omega_{b,i} q_{b,i}(t) + (m_c + m_p) \varphi_{b,i}(x_c) \\
 &\left(\ddot{x}_c \sum_{i=1}^n \varphi'_{t,i}(0) q_{t,i}(t) + 2\dot{x}_c \sum_{i=1}^n \varphi_{t,i}(0) \dot{q}_{t,i}(t) + x_c \sum_{i=1}^n \varphi_{t,i}(0) \ddot{q}_{t,i}(t) \right) \\
 &\quad + \sum_{i=1}^n \varphi_{b,i}(x_c) \ddot{q}_{b,i}(t) + (m_c + m_p) g \cdot \varphi_{b,i}(x_c) + (m_c + m_p) \\
 &\quad \left(\varphi'_{t,i}(0) \dot{q}_{t,i}(t) \varphi_{b,i}(x_c) \right) \left[\sum_{i=1}^n \varphi_{t,i}(0) \dot{q}_{t,i}(t) + \ddot{x}_c \right. \\
 &\quad \left. + \sum_{i=1}^n \varphi_{t,i}(0) \ddot{q}_{t,i}(t) W_z(x_c) + \sum_{i=1}^n \varphi_{t,i}(0) q_{t,i}(t) \dot{W}_z(x_c) \right] \\
 &\quad - m_p l \left[\ddot{\theta} \sin \theta \varphi_{b,i}(x_c) + \theta^2 \cos \theta \varphi_{b,i}(x_c) \right] = 0; \quad (18)
 \end{aligned}$$

$$\begin{aligned}
 &\ddot{\theta} + \left(\ddot{x}_c + \sum_{i=1}^n \varphi_{b,i}(x_c) q_{b,i}(t) \right) \cos \theta + g \sin \theta + l \cos \theta \sum_{i=1}^n \varphi_{t,i}(0) q_{t,i}(t) \\
 &- \sin \theta \left[x_c \sum_{i=1}^n \varphi'_{t,i}(0) \ddot{q}_{t,i}(t) + 2\dot{x}_c \sum_{i=1}^n \varphi'_{t,i}(0) \dot{q}_{t,i}(t) + \ddot{x}_c \sum_{i=1}^n \varphi'_{t,i}(0) q_{t,i}(t) \right. \\
 &\quad \left. + \sum_{i=1}^n \varphi'_{t,i}(0) \dot{q}_{t,i}(t) \varphi_{b,i}(x_c) \dot{q}_{t,i}(t) \right] = 0. \quad (19)
 \end{aligned}$$

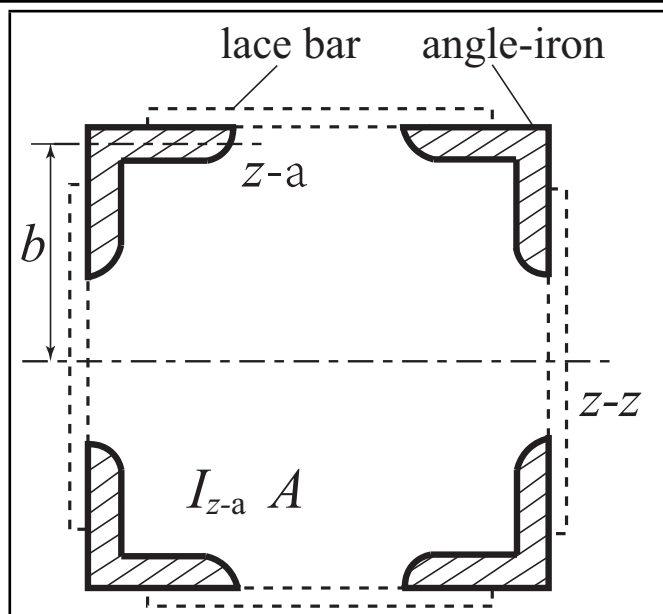


Figure 3. Cross-section of the tower.

The Eq. (17), (18) and (19) are defined as matrix equations about the generalized acceleration $\ddot{\eta}^*$, $\dot{\eta}^*$, and η^*

$$M\ddot{\eta}^* + C\dot{\eta}^* + K\eta^* = F u; \quad (20)$$

where the mass matrix is M , the damping matrix is C , and the stiffness matrix is K . The control force²⁰ matrix is $F = -\partial L / \partial u$, and more details are shown in the Appendix Eq. (A4), (A5) and (A6). The control quantity $u = [\ddot{x}_c]$. x_c , \dot{x}_c and W_z are included in the matrix C and K to affect the structures vibration and payload swing. In addition, the payload mass and rope length are also influencing factors.

3. MODAL ANALYSIS

3.1. Equivalent of the Tower

Due to the non-uniform distribution of stiffness in the lattice structure, the transverse shear on the lace bars and the effect of the lattice columns on the bending stiffness must be considered. According to the formula of Euler's critical force, the second moment of area of the tower and jib is calculated. The tower of the QTZ5613 flat-head tower crane is composed of the co-directional lace bar and four-limb lattice column. The cross-section of the tower is shown in Fig. 3.

The second moment of area for the cross-section to the $z-z$ axis generated by the lattice column without the lace bars is:

$$I_a = I_{z-a} + A \left(\frac{b}{2} \right)^2; \quad (21)$$

where b is the vertical distance from the $z-a$ axis of the angle-iron to the $z-z$ axis, A is the sum of the cross-sectional areas of the four angle-iron, and I_{z-a} is the sum of the second moment of the angle-iron to their own $z-a$ axis. The equivalent slenderness ratio of the lattice column is defined as:

$$\lambda_a = \frac{l_{0x}}{i_a} = \frac{\sqrt{I_a} A l_{0x}}{I_a}; \quad (22)$$

where l_{0x} is the sum of the projection lengths of the adjacent lace bar in the axis of the tower, the radius of gyration of tower

is i_a , and the slenderness ratio of the tower with the lace bar is:²¹

$$\lambda_h = \sqrt{\lambda_a^2 + 40 \frac{A}{A_1}}; \quad (23)$$

where A_1 is the sum of the cross-sectional areas of the lace bar. The equivalent second moment of the area for tower is defined as:¹⁶

$$I_{t,x} = \frac{(2l)^2 A}{\lambda_h} = I_a \frac{(2l)^2}{(l_{0x})^2 + 40 \frac{I_a}{A_1}}; \quad (24)$$

the moment of the cross-section of jib $I_{b,z}$ can also be calculated by the above formula.

3.2. Mode Shape of the Tower

After obtaining the moment of area for the cross-section, the i^{th} shape function of the tower is obtained by:

$$\varphi_{t,i}(z) = c_1 \sin(\beta_i z) + c_2 \cos(\beta_i z) + c_3 \sinh(\beta_i z) + c_4 \cosh(\beta_i z); \quad (25)$$

where c_1, c_2, c_3 and c_4 are the coefficients to be determined in the shape function, and c_3 is obtained by bringing the Eq. (25) into the regularization equation, which is shown in Appendix Eq. (A3). Similarly, the shape function of the jib $\varphi_{b,i}(x)$ can be obtained.

The bending moment and shear force disappear at the free end of the jib. However, the boundary conditions of the tower should consider the inertia of the slewing part as the end mass m_r , and the rotational inertia J_r of the slewing part. The boundary conditions of the tower end and the jib end are as follows:

$$\begin{cases} EI_{t,x} V_x''(z, t)|_{z=0} = -J_r \ddot{V}_x'(z, t)|_{z=0} \\ EI_{t,x} V_x'''(z, t)|_{z=0} = m_r \ddot{V}_x(z, t)|_{z=0} \end{cases}; \quad \begin{cases} EI_{b,z} W_z''(x, t)|_{x=l_b} = 0 \\ EI_{b,z} W_z'''(x, t)|_{x=l_b} = 0 \end{cases}; \quad (26)$$

substituting Eq.(26) into Eq. (25), yields

$$\xi_i = -\frac{\text{shs}(\beta_i l_t) + \frac{m_r}{m_t} \beta_i l_t [\cosh(\beta_i l_t) - \cos(\beta_i l_t)]}{\cosh(\beta_i l_t) + \cos(\beta_i l_t) + \frac{m_r}{m_t} \beta_i l_t [\text{shs}(\beta_i l_t)]}; \quad (27)$$

where $\xi_i = \frac{c_2}{c_3}$, shs represents $\sinh - \sin$. The characteristic root can be solved by the frequency equation,²² which is defined as:

$$A [c_1, c_2, c_3]^T = D c_4; \quad (28)$$

where A and D are the coefficient and constant matrix of the frequency equation, respectively. More details are shown in Appendix Eq. (A4). The first four Characteristic roots of the tower are $\beta_1 l_t = 0.765, \beta_2 l_t = 1.508, \beta_3 l_t = 4.780, \beta_4 l_t = 7.896$.

4. SIMULATION

With the four dominant eigenmodes used and hoisting speed $\dot{l} = 0$ in Eq. 20, differential equations with respect to η^* are built in the subroutine in Matlab software, which also includes the simulation of the trolley motion. The ode45 is a general-purpose solver for solving non-rigid differential equations. Thus, the main procedure uses the variable-step ode45

Table 1. Working condition.

Working condition	Trolley speed v_{\max}	Variable in trolley motion Mass of payload m_p	Rope length l
1	0.4	1800	18
2	0.8	1800	18
3	0.8	800	18
4	0.8	800	10

Table 2. QTZ5613 flat-head tower crane parameters.

Parameter	Value	Parameter	Value	Parameter	Value
m_t	350 kg/m	m_{cb}	159.3 kg/m	E	206 GPa
m_b	123.8 kg/m	l_{cb}	12.3 m	A	198.8 cm ²
l_t	23.8 m	m_{cw}	15130 kg	b	1680 mm
l_b	55.6 m	m_c	350 kg	$I_{t,x}$	0.014 m ⁴

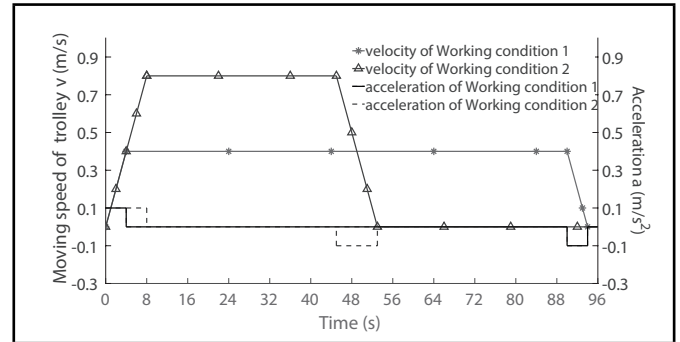


Figure 4. Motion patterns of the trolley.

solver to solve the states in the subroutine with an initial value of zero. The time span is 0 s to 120 s.

The relative tolerance (*rtol*) value is set to $1e^{-3}$, limiting the error to 0.1 %. The absolute tolerance (*atol*) value, $1e^{-6}$, is an acceptable error when the states are approaching zero. We obtain almost the same satisfactory results by reducing the *atol* value to $1e^{-7}$ in the second calculation to verify the accuracy of the simulation.

4.1. Working Condition

The simulation conditions are shown in Tab. 1. QTZ5613 flat-head tower crane parameters are shown in Tab. 2. In Tab. 1, in condition 1 and condition 2, the trolley moves from 5 m to 41 m from the tower centerline with an acceleration of 0.1 m/s^2 . The motion patterns of the trolley are shown in Fig. 4.

4.2. Effect of Trolley Speed

The radial swing angle and tower displacement under condition 1 and condition 2 are shown in Fig. 5 and Fig. 7, respectively. In order to illustrate the influence of radial motion on the payload swing, the phase trajectory of the payload swing is shown in Fig. 6.

In Fig. 5, in the acceleration phase, the swing angle has a consistent trend under condition 1 and condition 2. When the trolley reaches the rated speed, the payload enters the free-swinging state with an initial velocity and swing angle at 4 s and 8 s, respectively. During most of the deceleration phase, the direction of trolley deceleration is opposite to the payload swing, which leads to an increase in the swing angle. After braking, the payload enters the free swing state, and the swing period is 8.52 s.

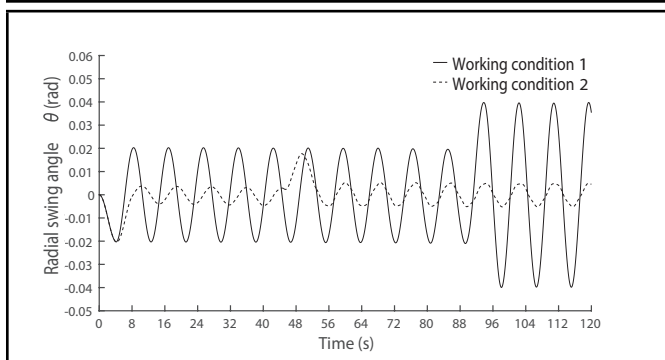


Figure 5. Radial swing angle under condition 1 and condition 2.

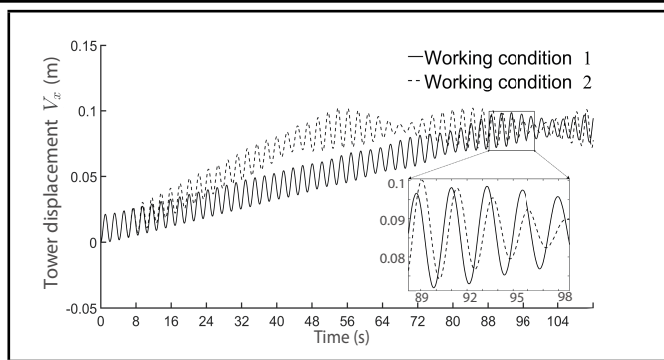


Figure 7. Tower displacement under condition 1 and condition 2.

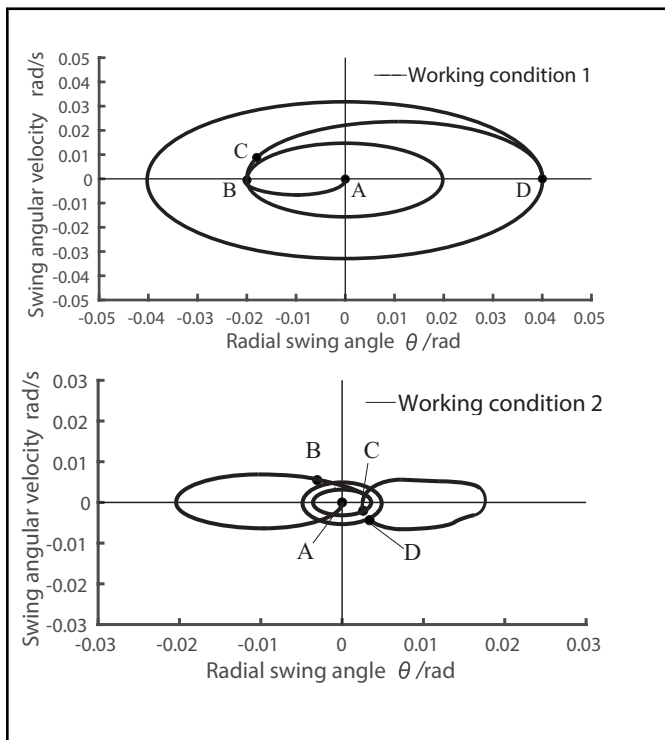


Figure 6. Phase trajectory of the payload swing.

In Fig. 6, the trolleys accelerate at point A, travel at a uniform speed at point B, decelerate at point C, and stop at point D. In Fig. 4.2, in the deceleration phase, the direction of the payload acceleration is in the opposite direction of the trolley movement, which intensifies the payload swing compared to the acceleration phase. The opposite is true in Fig. 4.2. The mutual cancellation of inertial forces makes the angle of the payload swing smaller than that of the acceleration phase. Therefore, in the deceleration phase, the direction of the payload acceleration is the main factor affecting the swing angle.

In Fig. 7, the tower displacement and period increase with the trolley speed. It is because, in the acceleration of the trolley, the swing angle relative to the equilibrium position is less than zero due to the inertia force. Thus, the direction of tension force exerted by the payload is always opposite to the direction of the trolley motion. The longer the acceleration time, the larger is the bending moment of the tower.

In addition, by the discrete Fourier transform (DFT), seen in Eq. (29), the sampled signal $V_x[n^*]$ of the tower displacement is expressed as a sum of different frequency components with $V_x[k^*]$ as coefficients and the spectrum of the tower vibrations

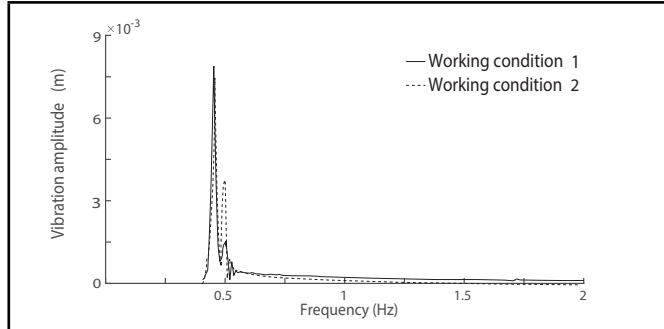


Figure 8. Spectrum of tower vibrations.

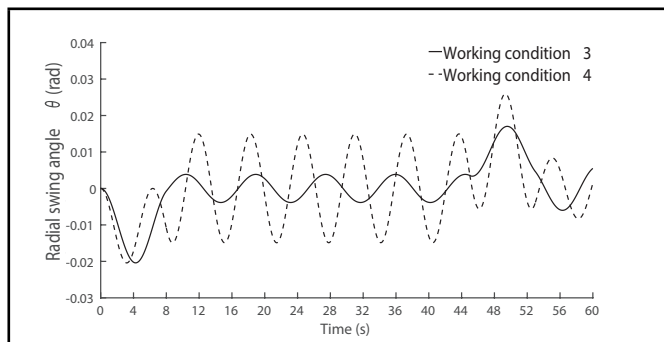


Figure 9. Radial swing angle under condition 3 and condition 4.

is shown in Fig. 8.

$$V_x[k^*] = \sum_{n^*=0}^{N^*-1} V_x[n^*] e^{j(2\pi/N^*)k^*n^*}; \quad (29)$$

where, j is the imaginary unit, n^* is the number of sampling points, and N^* is the number of points of the DFT transform whose points are the dimension of $V_x[n^*]$.

In Fig. 8, The first wave peaks of condition 1 and condition 2 appear at 0.45 Hz, which verifies the intrinsic frequencies corresponding to the first mode of the tower. The second wave peak appears at 0.49 Hz, and its amplitude is mainly influenced by the trolley speed.

4.3. Effect of Rope Length

The radial swing angle and tower displacement under working condition 3 and working condition 4 is shown in Fig.9 and Fig.10, respectively.

In Fig. 10, the length of the rope has almost no effect on the vibration characteristics of the tower. In Fig. 9, the maximum

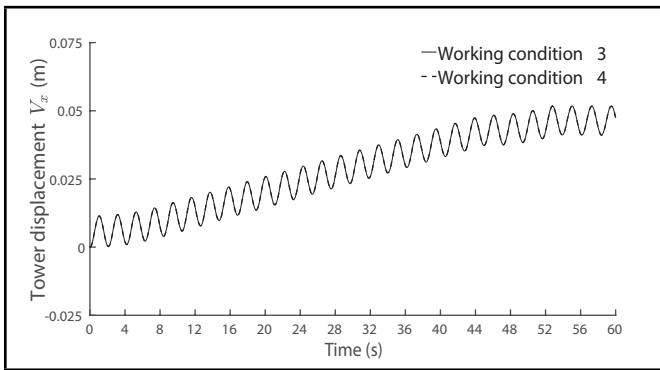


Figure 10. Displacement under condition 3 and condition 4.

swing angle of the payload is slightly different due to the different periods caused by the rope length. If the trolley starts and brakes quickly, there is the maximum input in the system, from which the maximum swing angle of the payload is quantified. Thus, the Eq. (19) is simplified to a linearized model of the payload swing:

$$\ddot{\theta} + \frac{g}{l}\theta = -\frac{\ddot{x}_c}{l}; \quad (30)$$

assuming that the initial states of the system is zero initial state, and the solution of Eq. (30) is obtained:

$$\theta(t) = -\frac{\ddot{x}_c \omega_n^2 t}{2g}; \quad (31)$$

where ω_n is the intrinsic frequency of load swing, the payload swing angle is $\lim_{t \rightarrow 0} \theta(t) = 0$, and the angular velocity is $\lim_{t \rightarrow 0} \dot{\theta}(t) = -v_{max}/l$, the maximum speed is $\theta_{max} = -v_{max}/l$. According to the law of energy conservation, the estimated maximum angle is:

$$\theta_{max} = \frac{v_{max}}{g\sqrt{l}}; \quad (32)$$

where the maximum angles are 0.020 rad and 0.026 rad under condition 3 and condition 4, respectively. The calculation results are consistent with the simulation results of Fig. 9. If the rope length and trolley speed satisfy $l < (18v_{max})^2 / (\pi^2 g)$, θ is greater than 10° , at which time the assumptions of the linearized model are not satisfied, that is, the linearized model has a large error.

4.4. Effect of Mass

In Eq. (19), the payload mass is independent of both the swing angle and period, which is consistent with the findings of Jerman.²³ So the swing characteristics of condition 3 are the same as condition 2. The tower displacement in condition 2 and condition 3 is shown in Fig. 11.

The displacement and period of the tower increase coincide with the increase in payload mass, which indicates that the payload mass is the main factor affecting the vibration characteristics of the tower.

5. EXPERIMENTAL VERIFICATION

5.1. Experiment Design

The experiment system is implemented on the full-scale QTZ5613 flat-head tower crane. The experiment system in-

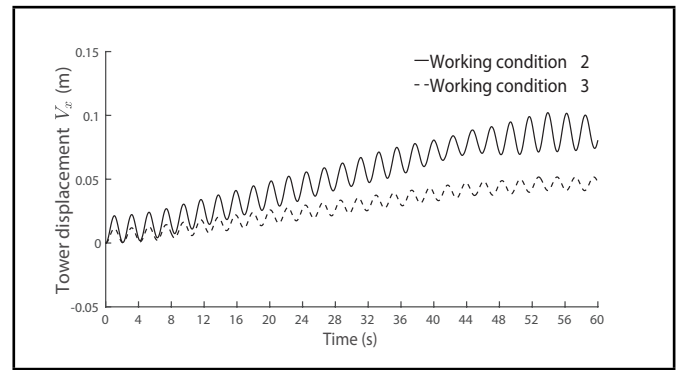


Figure 11. Displacement under condition 2 and condition 3.

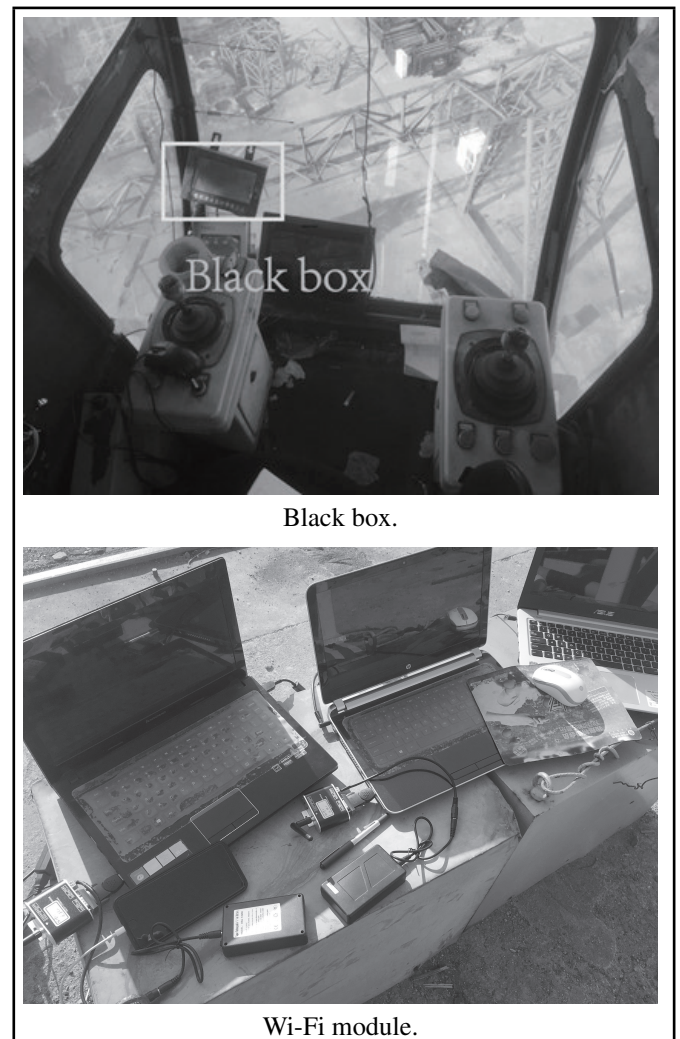


Figure 12. Installation of working condition experiment subsystem.

cludes three parts: the working condition experiment subsystem, the vibration experiment subsystem, and the payload swing experiment subsystem.

A monitoring black box, i.e., the working condition experiment subsystem, is installed on the crane cabin to obtain the operational status of the tower crane. Measurement data from each subsystem is transmitted directly to the terminal via the Wi-Fi module. The installation of working condition experiment subsystem is shown in Fig. 12.

For the tower vibration experiment, the tower tilt angle monitoring adopts the MSH-517 static inclinometer sensor (shown

in Fig. 5.1). It selects the turning angle at the top of the tower as the observation object. The accuracy of the sensor is 0.005° , and the average value of the sensor measurement angle (three times) is taken as the final result to ensure reliability. The static inclinometer sensors 1 and 2 are installed on the rotating platform and the fixed platform, respectively, to measure the tilt angle of the tower around x -axis and y -axis, shown in Fig. 5.1.

For the jib vibration experiment, two laser rangefinders are installed and positioned at the end of the jib to measure the vertical distance from the jib to the ground, as shown in Fig. 5.1. The laser rangefinders have to point vertically downward to the ground, and a white reflector is laid flat on the ground to ensure the accuracy of the measurement, as shown in Fig. 5.1.

The installation of the payload swing experiment subsystem is shown in Fig. 14.

The dynamic inclinometer is fixed on the hook to measure the swing angle. The dynamic inclinometer is assembled with an accelerometer and gyroscope, which can accurately output the swing angle of the payload. The final measured data are the average of three experimental results. The sensor selection and installation reference the work of Feng.¹⁵

5.2. Experimental Verification of Dynamic

The comparison of the simulation results and experimental data is shown in Fig.15.

5.2.1. Effect of the Speed

Experimental comparisons of the tower displacement under condition 1 and condition 2 are shown in Fig. 5.2.1 and Fig. 5.2.1, respectively. The vibration characteristics of the tower in the experiment are basically the same as the simulation results. Otherwise, the tower vibration belongs to a high-frequency response. The static inclinometer sensor has low sensitivity to this high-frequency input signal, leading to a specific difference in the value of the experiment data.

Experimental comparisons of the payload swing angle under condition 1 and condition 2 are shown in Fig. 5.2.1 and Figure. 5.2.1, respectively.

The swing characteristics of the payload in the experiment are basically consistent with the simulation results. Due to the high payload above the ground, the experimental data show some fluctuations influenced by the wind.

5.2.2. Effect of the Mass

Experimental comparisons of vibration characteristics of the tower under condition 3 are shown in Fig.5.2.1. The vibration characteristics of the tower are basically the same as the simulation results in Fig.11.

5.2.3. Effect of the Rope Length

Experimental comparisons of the payload swing angle under condition 4 are shown in Fig. 5.2.1. The comparison shows that the payload swing characteristics and simulation results in Fig. 9 are basically the same. However, the rope in the experiment is flexible, which means that the length of the rope will change periodically, resulting in some differences between the experimental data and the simulation results.

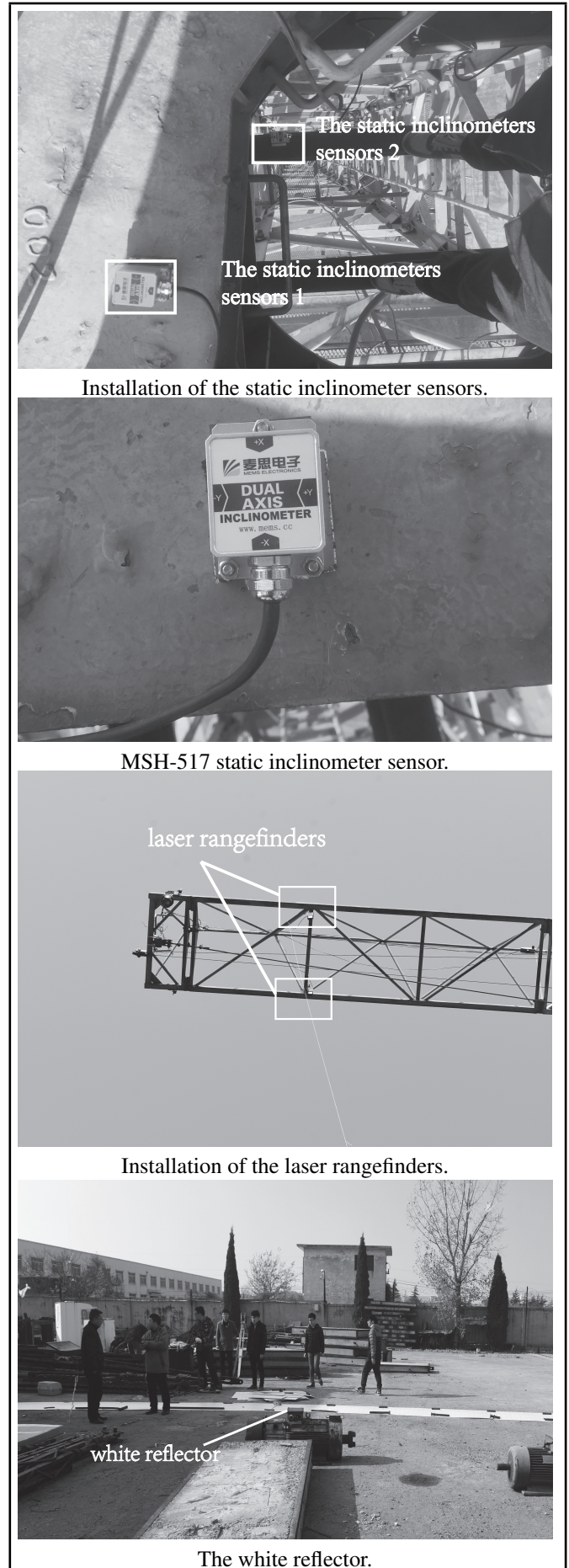


Figure 13. Installation of the vibration experiment subsystem.



Figure 14. Installation of payload swing experiment subsystem.

6. CONCLUSIONS

This paper presents an analytical method for simulating the tower vibration, jib vibration, and payload swing in radial motion. The effects of the dynamic parameters on the tower vibration and the payload swing characteristics were investigated by simulation and experiment.

The results of this research showed that the displacement and period of the tower are directly proportional to the payload mass, trolley speed, and jib vibration, while the rope length does not have a significant effect on the tower vibration. The acceleration direction of the payload and the rope length are the main factors affecting the payload swing angle. The effectiveness of the tower crane model subjected to an elastic jib and the tower equivalence method was indirectly verified. The work helps improve the operational reliability in the design stage of tower cranes. Vibration suppression will be conducted in our future research.

REFERENCES

- 1 L. Zhang, J. Wu, and D. Meng, A method for quantifying automobile brake creep groan intensity based on friction-induced vibration and noise, *Shock and Vibration*, **2021**, (2021). <https://doi.org/10.1155/2021/4885330>.
- 2 N. D. Zrnic, S. M. Bosnjak, V. M. Gasic, M. A. Arsic, and Z. D. Petkovic, Failure analysis of the tower crane counterjib, *Procedia engineering*, **10**, 2238–2243, (2011). <https://doi.org/10.1016/j.proeng.2011.04.370>
- 3 C. S. Oliveira and P. Correia, “Comparison of the seismic and wind analyses of two tower cranes,” *Journal of Vibroengineering*, **23**(4), 956–975, (2021). <https://doi.org/10.21595/jve.2021.21649>
- 4 M. H. El Ouni, N. Ben Kahla, S. Islam, and M. Jameel, A smart tower crane to mitigate turbulent wind loads, *Structural Engineering International*, **31**(1), 18–29, (2021). <https://doi.org/10.1080/10168664.2019.1668334>
- 5 Y. Ushio, T. Saruwatari, and Y. Nagano, Elastoplastic fem analysis of earthquake response for the fieldbolt joints

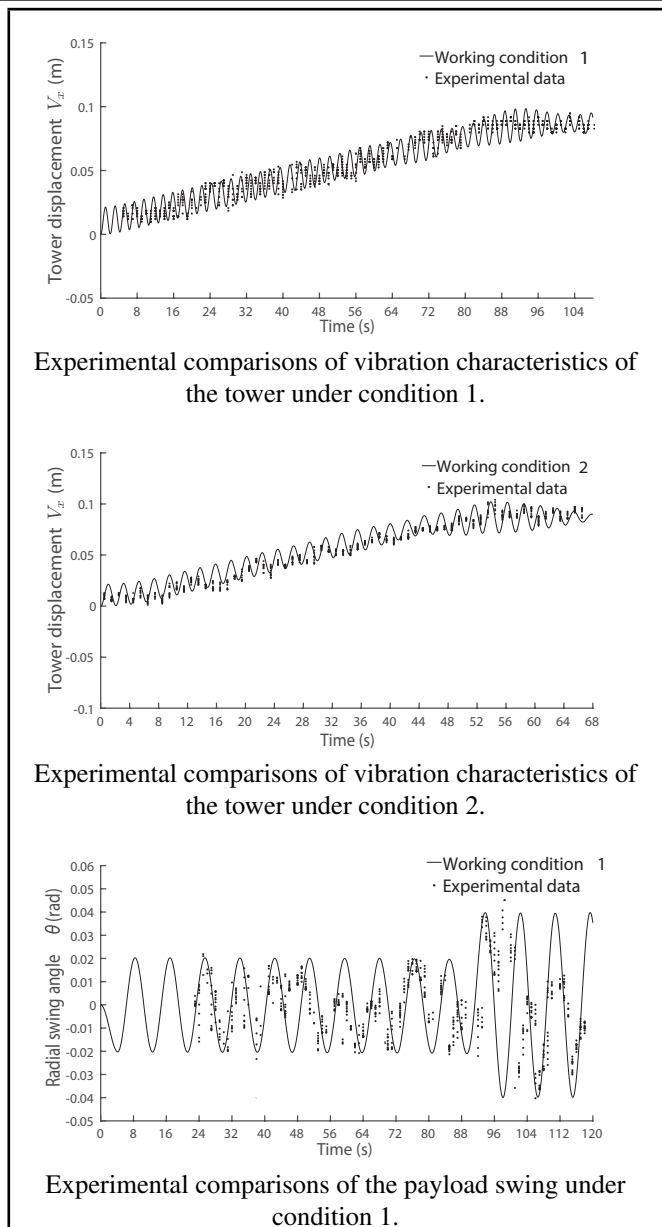


Figure 15. The comparison of the simulation results and experimental data.

of a tower-crane mast, *Advances in Computational Design*, **4**(1), 53–72, (2019). <https://doi.org/10.2991/ameii-16.2016.207.19>

- 6 W. Chen, X. Qin, Z. Yang, and P. Zhan, Wind-induced tower crane vibration and safety evaluation, *Journal of Low Frequency Noise, Vibration and Active Control*, **39**(2), 297–312, (2020). <https://doi.org/10.1177/1461348419847306>
- 7 Zrnic, N. D. and Gavsic, V. M. and Bosnjak, Srdjan M, Dynamic responses of a gantry crane system due to a moving body considered as moving oscillator, *Archives of Civil and Mechanical Engineering*, **15**(1), 243–250, (2015). <https://doi.org/10.1016/j.acme.2014.02.002>
- 8 I. Gerdemeli, I. Esen, and D. Ozer, Dynamic response of an overhead crane beam due to a moving mass using moving finite element approximation, in *Key Engineering Materials*, **450**, 2011, 99–102, <https://doi.org/10.4028/www.scientific.net/kem.450.99>

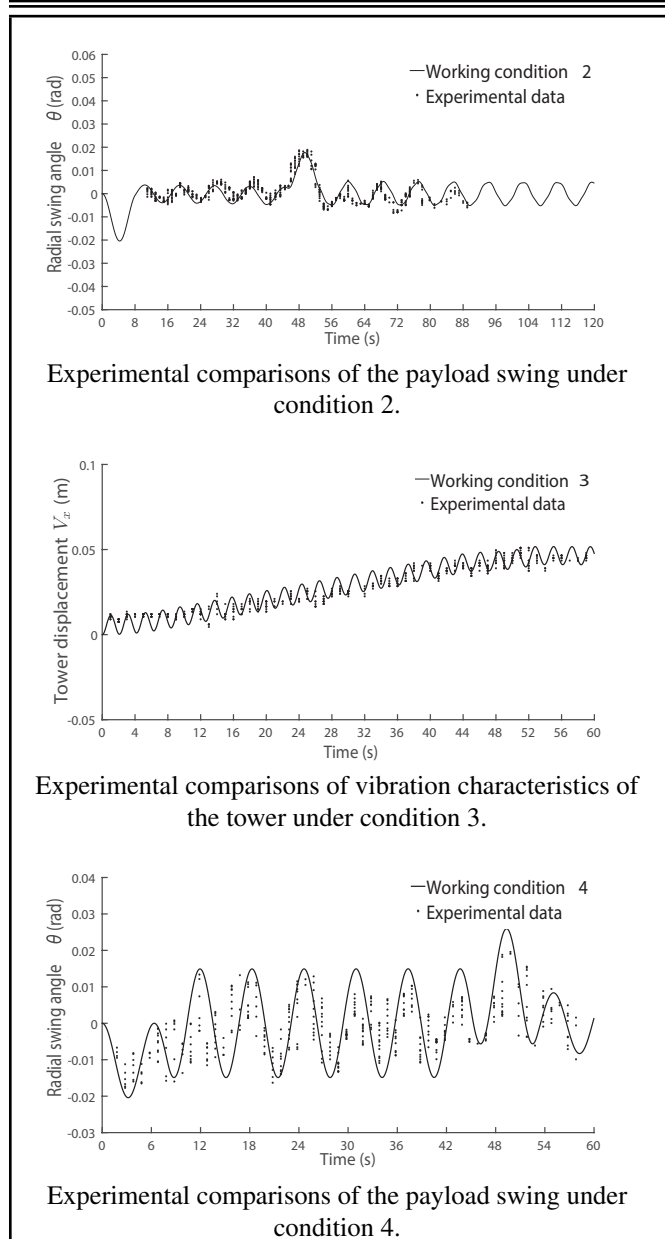


Figure 16. The comparison of the simulation results and experimental data (continued).

- ⁹ V. Gasic, N. Zrnic, A. Obradovic, and S. Bosnjak, Consideration of moving oscillator problem in dynamic responses of bridge cranes, *FME Transactions*, **39**(1), 17–24, (2011). <https://doi.org/10.5937/fmet1403177s>
- ¹⁰ S. E. Azam, M. Mofid, and R. A. Khoraskani, Dynamic response of timoshenko beam under moving mass, *Scientia Iranica*, **20**(1), 50–56, (2013). <https://doi.org/10.1016/j.scient.2012.11.003>
- ¹¹ C. Debeleac, On nonlinear dynamics of dragline bucket subjected to flexible linkages, *Romanian Journal of Acoustics and Vibration*, **11**(2), 150, (2014). <https://www.researchgate.net/publication/292508403>
- ¹² C. Debeleac and S. Nastac, Computational assessments on dragline bucket oscillations, *Romanian Journal of Acoustics and Vibration*, **15**(2), 149–157, (2018). <http://rjav.sra.ro/index.php/rjav/article/view/78>
- ¹³ C. Debeleac, S. Nastac, and G. D. Musca, Experimental investigations regarding the structural damage monitoring of strands wire rope within mechanical systems, *Materials*, **13**(15), 3439, (2020). <https://doi.org/10.3390/ma13153439>
- ¹⁴ F. Rauscher and O. Sawodny, An elastic jib model for the slewing control of tower cranes, *IFAC PapersOnLine*, **50**(1), 9796–9801, (2017). <https://doi.org/10.1016/j.ifacol.2017.08.886>
- ¹⁵ R. Feng, E. Zhang, and M. Dong, Jib vibration and payload swing of tower cranes in the case of trolley motion, *Arabian Journal for Science and Engineering*, **46**(12), 12 179–12 191, (2021). <https://doi.org/10.1007/s13369-021-05804-3>
- ¹⁶ F. Rauscher and O. Sawodny, Modeling and control of tower cranes with elastic structure, *IEEE Transactions on Control Systems Technology*, **29**(1), 64–79, (2020). <https://doi.org/10.1109/tcst.2019.2961639.20>
- ¹⁷ J. Ye and J. Huang, Analytical analysis and oscillation control of payload twisting dynamics in a tower crane carrying a slender payload, *Mechanical Systems and Signal Processing*, **158**, 107763, (2021). <https://doi.org/10.1016/j.ymsp.2021.107763>
- ¹⁸ G. Orzechowski, J. L. Escalona, O. Dmitrochenko, N. Mohammadi, and A. M. Mikkola, Modeling viscous damping for transverse oscillations in reeving systems using the arbitrary lagrangian–eulerian modal approach, *Journal of Sound and Vibration*, **534**, 117009, (2022). <https://doi.org/10.1016/j.jsv.2022.117009>
- ¹⁹ C. Debeleac and S. Vlase, Experimental assessments on the evaluation of wire rope characteristics as helical symmetrical multi-body ensembles, *Symmetry*, **12**(8), 1231, (2020). <https://doi.org/10.3390/sym12081231>
- ²⁰ D. Fujioka and W. Singhose, Input-shaped model reference control of a nonlinear time varying double-pendulum crane, in *2015 10th Asian Control Conference (ASCC)*, **2015**, 1–6, (2015). <https://doi.org/10.1109/ascc.2015.7244565>.
- ²¹ S. administration of The People’s Republic Of China, Design rules for cranes (gb/t 3811–2008), 2008, <https://openstd.samr.gov.cn/bz/gk/gb/newGbInfo?hcno=4F6CEE797EBFF2A3E3B96DC198AE18DA>
- ²² J. Burns, E. Cliff, Z. Liu, and R. D. Spies, On coupled transversal and axial motions of two beams with a joint, *Journal of Mathematical Analysis and Applications*, **339**(1), 182–196, (2008). <https://doi.org/10.1016/j.jmaa.2007.06.047>
- ²³ B. Jerman, P. Podrzaj, and J. Kramar, “An investigation of slewing-crane dynamics during slewing motion—development and verification of a mathematical model, *International Journal of Mechanical Sciences*, **46**(5), 729–750, (2004). <https://doi.org/10.1016/j.ijmecsci.2004.05.006>

APPENDIX

$$T_z = \begin{bmatrix} \cos \psi & -\sin \psi & 0 \\ \sin \psi & \cos \psi & 0 \\ 0 & 0 & 1 \end{bmatrix} T_y = \begin{bmatrix} \cos \gamma & 0 & \sin \gamma \\ 0 & 1 & 0 \\ -\sin \gamma & 0 & \cos \gamma \end{bmatrix} T_G = \begin{bmatrix} 0 & 0 & \cos \phi \sin \theta \\ 0 & 0 & \sin \phi \\ 0 & 0 & \cos \phi \cos \theta \end{bmatrix} \tag{A1}$$

$$K_{\text{tol}} = \frac{1}{2} \sum_{i=1}^n [\dot{q}_{t,i}(t)]^2 + \frac{1}{2} m_c \left\{ \left[\sum_{i=1}^n \varphi_{t,i}(0) \dot{q}_{t,i}(t) + \dot{x}_c + \sum_{i=1}^n \varphi'_{t,i}(0) \dot{q}_{t,i}(t) W_z(x_c) \right]^2 + \left[x_c \sum_{i=1}^n \varphi'_{t,i}(0) \dot{q}_{t,i}(t) + \dot{x}_c \sum_{i=1}^n \varphi_{t,i}(0) q_{t,i}(t) + \sum_{i=1}^n \varphi_{b,i}(x_c) \dot{q}_{b,i}(t) \right]^2 \right\} + \frac{1}{2} m_p \left\{ \left[x_c \sum_{i=1}^n \varphi'_{t,i}(0) q_{t,i}(t) + \dot{x}_c \sum_{i=1}^n \varphi'_{t,i}(0) q_{t,i}(t) + \sum_{i=1}^n \varphi_{b,i}(x_c) q_{b,i}(t) + l \sin \theta \dot{\theta} \right]^2 + \left[\sum_{i=1}^n \varphi_{t,i}(0) \dot{q}_{t,i}(t) + \dot{x}_c + \sum_{i=1}^n \varphi'_{t,i}(0) \dot{q}_{t,i}(t) W_z(x_c) - l \cos \theta \dot{\theta} \right]^2 \right\} + \frac{1}{2} \sum_{i=1}^n [\dot{q}_{b,i}(t)]^2 \tag{A2}$$

$$\frac{1}{2} \sum_{i=1}^n \sum_{j=1}^n \dot{q}_{t,i} \dot{q}_{t,j} \left[\int_{-l_t}^0 m_t \varphi_{t,i}(z) \varphi_{t,j}(z) dz + (m_b + m_{cb} + m_{cw}) \mu_{ij} + \left(J_r + \int_0^{l_b} m_b W_z^2(x) dx \right) \mu''_{ij} \right] = \frac{1}{2} \sum_{i=1}^n \sum_{j=1}^n \dot{q}_{t,i} \dot{q}_{t,j} \tag{A3}$$

$$\frac{1}{2} \sum_{i=1}^n \sum_{j=1}^n \dot{q}_{b,i} \dot{q}_{b,j} \left[\int_0^{l_b} m_b \varphi_{b,i}(x) \varphi_{b,j}(x) dx + m_b l_b \varphi_{b,i}(x) \varphi_{b,j}(x) V'_x(0)^2 \right] = \frac{1}{2} \sum_{i=1}^n \sum_{j=1}^n \dot{q}_{b,i} \dot{q}_{b,j}$$

where, $\varphi_{t,i}(0) \varphi_{t,j}(0) = \mu_{ij}$, $\varphi_{t,i}(0)' \varphi_{t,j}(0)' = \mu''_{ij}$.

$$A = \begin{pmatrix} 0 & 1 & 0 \\ -\sin(\tau_i) - I_1 \cos(\tau_i) & -\cos(\tau_i) + I_1 \sin(\tau_i) & \sinh(\tau_i) - I_1 \cosh(\tau_i) \\ -\cos(\tau_i) + I_2 \sin(\tau_i) & \sin(\tau_i) + I_2 \cos(\tau_i) & \cosh(\tau_i) + I_2 \sinh(\tau_i) \end{pmatrix} D = \begin{pmatrix} -1 & 0 \\ I_1 \sinh(\tau_i) - \cosh(\tau_i) \\ -I_2 \cosh(\tau_i) + \sinh(\tau_i) \end{pmatrix} \tag{A4}$$

where, $(J_r \frac{\beta_i^3}{m_t}) = I_1$, $(m_r \frac{\beta_i}{m_t}) = I_2$, $\beta_i l_t = \tau_i$.

$$M = \begin{bmatrix} 1 + k(\mu_{11} + x_c^2 \mu''_{11}) & \cdots & 1 + k(\mu_{1j} + x_c^2 \mu''_{1j}) & \cdots & 1 + k(\mu_{1n} + x_c^2 \mu''_{1n}) & m_p l x_c (\cos \theta \varphi_{t,1} - \sin \theta \varphi'_{t,1}) \\ \vdots & \ddots & \vdots & \ddots & \vdots & \vdots \\ 1 + k(\mu_{i1} + x_c^2 \mu''_{i1}) & \cdots & 1 + k(\mu_{ii} + x_c^2 \mu''_{ii}) & \cdots & 1 + k(\mu_{in} + x_c^2 \mu''_{in}) & m_p l x_c (\cos \theta \varphi_{t,i} - \sin \theta \varphi'_{t,i}) \\ \vdots & \ddots & \vdots & \ddots & \vdots & \vdots \\ 1 + k(\mu_{n1} + x_c^2 \mu''_{n1}) & \cdots & 1 + k(\mu_{nj} + x_c^2 \mu''_{nj}) & \cdots & 1 + k(\mu_{nn} + x_c^2 \mu''_{nn}) & m_p l x_c (\cos \theta \varphi_{t,n} - \sin \theta \varphi'_{t,n}) \\ 0 & \cdots & 0 & \cdots & 0 & l \end{bmatrix} \tag{A5}$$

$$C = \begin{bmatrix} (c^* + q_{b,1}^2) \mu''_{11} & \cdots & (c^* + q_{b,1}^2) \mu''_{ij} & \cdots & (c^* + q_{b,1}^2) \mu''_{in} & -m_p \varphi'_{t,1} l x_b \cos \theta \\ \vdots & \ddots & \vdots & \ddots & \vdots & \vdots \\ (c^* + q_{b,i}^2) \mu''_{i1} & \cdots & (c^* + q_{b,i}^2) \mu''_{ii} & \cdots & (c^* + q_{b,i}^2) \mu''_{in} & -m_p \varphi'_{t,i} l x_b \cos \theta \\ \vdots & \ddots & \vdots & \ddots & \vdots & \vdots \\ (c^* + q_{b,n}^2) \mu''_{n,1} & \cdots & (c^* + q_{b,n}^2) \mu''_{ni} & \cdots & (c^* + q_{b,n}^2) \mu''_{nn} & -m_p \varphi'_{t,n} l x_b \cos \theta \\ 0 & \cdots & 0 & \cdots & 0 & 0 \end{bmatrix} \tag{A6}$$

$$K = \begin{bmatrix} \omega_1^2 + k \mu''_{11} \ddot{x}_c x_c & \cdots & k \mu''_{1n} \ddot{x}_c x_c & 0 \\ \vdots & \ddots & \vdots & \vdots \\ \vdots & \omega_i^2 + k \mu''_{ii} \ddot{x}_c x_c & \vdots & \vdots \\ k \mu''_{n1} \ddot{x}_c x_c & \cdots & \omega_n^2 + k \mu''_{nn} \ddot{x}_c x_c & 0 \\ 0 & \cdots & 0 & 0 \end{bmatrix} F = \begin{bmatrix} -k \varphi_{t,1}(0) \\ \vdots \\ -k \varphi_{t,i}(0) \\ \vdots \\ -k \varphi_{t,n}(0) \\ \sin \theta \left(\sum_{i=1}^n \varphi'_{t,i}(0) q_{t,i}(t) \right) \end{bmatrix} \tag{A7}$$

where, $c^* = 2k(\dot{x}_c + W_z(x_c)^2)$, $m_c + m_p = k$.